Single-Dipole and Dual-Dipole Inverse Solutions in Electrocardiography

Vojko Jazbinšek and Rok Hren
Institute of Mathematics, Physics and Mechanics, Ljubljana, Slovenia
Email: vojko.jazbinsek@imfm.si

***Abstract*—In this study, we closely examined the performance of inverse solution in terms of equivalent dipole source model. To simulate potential distribution on the body surface, we employed an analytical model of a single current dipole (or a pair of current dipoles) placed within the homogeneous isotropic volume conductor consisting of two non-concentric spheres. Using these data, we evaluated the accuracy of recovering both location and orientation of the single or dual dipole sources. In total, we examined 24 different dipole locations and found that the location of fitted single and dual current dipoles virtually coincided with the original source for high S/N ratios.**

We extended investigation to more complex geometry, where a computer model of the human ventricular myocardium was used to simulate activation sequences initiated at eight sites positioned on the epicardial surface of the atrio-ventricular ring. From these sequences, 117-lead body surface potentials were simulated on a realistic torso surface and were then used to localize single and dual accessory pathways employing single or dual equivalent dipoles. Average localization errors were 5 and 12 mm for the single and the dual accessory pathways, respectively, what could be useful additional information prior to electrophysiological study.

I. INTRODUCTION

Mathematical modeling of both source and volume conductor remains one of the prerequisites for any quantitative interpretation of electrocardiographic data. One of the most often used approaches to solving the inverse problem in electrocardiography involves calculating the position and moment of an equivalent single dipole source in the model of the human torso [1]–[3]. It has been widely recognized that the equivalent single dipole approximation is adequate only when cardiac activity is confined to a single, relatively small volume, e.g. arising owing to ectopic foci and accessory pathways between the atria and ventricles. It thus appears intuitive that, in the presence of multiple ventricular events, more complex equivalent generators consisting of two [4] or more equivalent dipoles would achieve better accuracy and therefore a better understanding of the underlying cardiac process. This is particularly important when localizing those accessory atrioventricular connections presented in Wolff-Parkinson-White (WPW) syndrome that consist of dual parallel fibers [5]. As radiofrequency ablations of such multiple aberrant pathways are considered difficult [6], it is desirable to obtain as much information as possible regarding the accessory pathways location and anatomy (a single pathway as against multiple ones) prior to the invasive procedure.

In this simulation study, we explored the possibility that approximation by two dipoles could be used to localize regional activation of dual accessory pathways. In the first part, we employed simple analytical conducting sphere model that may serve as an efficient tool in examining performance of electrocardiographic inverse solution in terms of models, which use either single current dipoles or dual current dipoles. In the second part, we employed an anatomical computer model of the human ventricular myocardium to simulate activation sequences initiated on the epicardial surface of the atrio-ventricular ring, and from these sequences we simulated body surface potentials on a realistic torso surface. The results may be useful in providing additional means for assisting electrophysiology study during radiofrequency ablations of dual accessory pathways.

II. METHODS

A. Conducting sphere model

In the first part of this study, we used a pair of homogeneous and isotropic non-concentric spheres and placed either a single current dipole or a pair of two dipoles inside of the smaller sphere. The potentials at an arbitrary point $\vec{r}$ inside a sphere with radius R and conductivity σ can be calculated analytically [7]

$$\begin{aligned} V(\vec{r}) &= \frac{\vec{p}}{4\pi\sigma R^3}\cdot\left\{\frac{R^3(\vec{r}-\vec{r}_p)}{|\vec{r}-\vec{r}_p|^3}+\frac{1}{r_{pi}^3}\left(\vec{r}-\frac{r^2}{R^2}\vec{r}_p\right)\right.\\ &+\left.\frac{1}{r_{pi}}\left[\vec{r}+\frac{(\vec{r}\cdot\vec{r}_p)\vec{r}-r^2\vec{r}_p}{R^2(r_{pi}+1)-(\vec{r}\cdot\vec{r}_p)}\right]\right\}, \qquad (1)\end{aligned}$$

where $\vec{p}$ and $\vec{r}_p$ are dipole moment and position, and

$$r_{pi}=\left[1+\left(\frac{r_p r}{R^2}\right)^2-2\frac{(\vec{r}\cdot\vec{r}_p)}{R^2}\right]^{1/2}. \qquad (2)$$

Note, that in the original formula (13) in [7], the $(\vec{r}\cdot\vec{r}_p)$ is expressed as $(r_p r\cos\varphi)$, where φ is the angle between $\vec{r}$ and $\vec{r}_p$. For the surface potential, $r\equiv R$, $Rr_{pi}=|\vec{R}-\vec{r}_p|$, (1) is simplified to formula derived by Brody et al. [8]

$$\begin{aligned} V(\vec{R}) &= \frac{\vec{p}}{4\pi\sigma R^3}\cdot\left\{2\frac{R^3(\vec{R}-\vec{r}_p)}{|\vec{R}-\vec{r}_p|^3}\right.\\ &+\left.\frac{R}{|\vec{R}-\vec{r}_p|}\left[\vec{R}+\frac{(\vec{R}\cdot\vec{r}_p)\vec{R}-R\vec{r}_p}{|\vec{R}-\vec{r}_p|+R-r_p\cos\varphi}\right]\right\}. \qquad (3)\end{aligned}$$

We approximated the thoracic surface by the homogeneous conducting sphere with the unity radius ($R=1$), and the epicardial surface by a smaller sphere with a radius of $R_{\mathrm{E}}=0.5$, positioned eccentrically

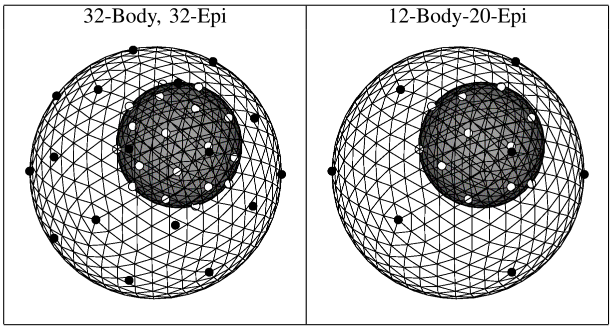

Fig. 1. Lead systems used in the fitting procedure: i) 32-leads on the body, ii) 32-leads on the epicardium and iii) combination of 12-leads on the body and 20-leads on the epicardium. Leads on the body (outer sphere) are denoted with •, leads on the epicardium(inner sphere) are denoted with ○.

$\vec{r}_E = (0.1, -0.2, 0.3)$. The body and the epicardial surfaces were tessellated using 1280 and 720 triangles (642 and 362 nodes), respectively. The tessellation of the body surfaces was generated by refinement of icosahedron in four steps and the epicardial surface was generated by refinement of truncated icosahedron in two steps. In this paper, we tested three electrode systems, each having 32 leads, see Fig. 1.

We put the single dipole source model in the total of 24 locations, 12 in nodes of icosahedron positioned near the center of the body surface and 12 in nodes of icosahedron positioned near the center of the epicardial surface, see Table I. In each of the positions, we put 3 single current dipoles pointing along axes of the Cartesian coordinate system, which gives total of 72 single dipole sources.

For the dual dipole model, we combined node positions of both source icosahedrons from Table I to construct 12 most close positioned pairs (mean distance 0.178 ± 0.069), 12 most distant positioned pairs (mean distance 0.696 ± 0.026), and 12 pairs of corresponding nodes shifted by $\vec{r}_E$ (median, $||\vec{r}_E|| = 0.374$), see Table II. In each of the pairs, we put either 3 parallel or anti-parallel or perpendicular dipoles pointing along axes of the Cartesian coordinate system. For each type of distance (close, median, distant) and each type of direction (parallel, anti-parallel, perpendicular), we therefore obtain 36 dual dipole sources.

For all single and dual dipole sources, we calculated potential maps on three lead systems from Fig. 1 using (1). In order to test the inverse solution, we added to the analytically calculated maps 7 different noise levels (*S/N*=10,15,. . . ,40 dB), where

$$S/N = 20 \log_{10} \frac{\mathrm{RMS(signal)}}{\mathrm{RMS(noise)}} \,. \tag{4}$$

For each analytically calculated map and for each noise level, we generated 10 different random noise distributions and performed the inverse solutions either for a single-dipole model or dual-dipoles model.

TABLE I. RELATIVE POSITIONS OF SINGLE-DIPOLES*

1st icosahedron			2nd icosahedron		
N_1	ρ_B	ρ_E	N_2	ρ_B	ρ_E
1	0.340	0.078	1	0.714	0.681
2	0.340	0.418	2	0.684	0.681
3	0.210	0.482	3	0.557	0.421
4	0.400	0.388	4	0.750	0.800
5	0.210	0.494	5	0.554	0.421
6	0.340	0.441	6	0.680	0.681
7	0.340	0.683	7	0.628	0.681
8	0.210	0.719	8	0.489	0.421
9	0.000	0.748	9	0.374	0.000
10	0.340	0.692	10	0.626	0.681
11	0.210	0.732	11	0.484	0.421
12	0.210	0.840	12	0.438	0.421

* Dipoles are positioned in nodes of two icosahedrons, which have same dimension defined by circumsribed sphere radius of 0.3 and are positioned inside body surface ($\rho_B = r_p/R_B$, outer sphere with radius $R_B = R = 1$) positioned in the center of Cartesian coordinate system, and inside epicard surface ($\rho_E = ||\vec{r}_p - \vec{r}_E||/R_E$, inner sphere with radius $R_E = 0.5$) shifted by $\vec{r}_E = (0.1, -0.2, 0.3)$.

TABLE II. DUAL-DIPOLES POSITIONS**

close (0.178±0.069)		median(0.374)		distant(0.696±0.026)	
(N_1,N_2)	Δr_{12}	(N_1,N_2)	Δr_{12}	(N_1,N_2)	Δr_{12}
(1,9)	0.039	(1,1)	0.374	(9,4)	0.745
(4,12)	0.039	(2,2)	0.374	(12,1)	0.739
(2,8)	0.165	(3,3)	0.374	(9,1)	0.714
(6,11)	0.165	(4,4)	0.374	(12,4)	0.714
(4,9)	0.194	(5,5)	0.374	(9,2)	0.684
(2,9)	0.209	(6,6)	0.374	(11,4)	0.684
(4,11)	0.209	(7,7)	0.374	(8,4)	0.680
(4,8)	0.220	(8,8)	0.374	(9,6)	0.680
(6,9)	0.220	(9,9)	0.374	(11,2)	0.680
(1,11)	0.227	(10,10)	0.374	(11,1)	0.678
(2,12)	0.227	(11,11)	0.374	(12,2)	0.678
(1,5)	0.230	(12,12)	0.374	(8,1)	0.675

**Pairs (N_1,N_2) of positions from the 1st and the 2nd icosahedron defined in Table I, Δr_{12} is a distance betveen the two dipoles.

As a measure of localization accuracy, we used the distance between the recovered location(s) and original location(s) of dipole(s). In addition, we also calculated relative errors between noisy $\mathbf{V}_n$ and fitted $\mathbf{V}_f$ maps ($\mathrm{RE_{fn}}$), and between analytical $\mathbf{V}_a$ and fitted maps ($\mathrm{RE_{fa}}$):

$$\mathrm{RE_{fn}} = \frac{||\mathbf{V}_f - \mathbf{V}_n||_2}{||\mathbf{V}_n||_2} \,, \; \mathrm{RE_{fa}} = \frac{||\mathbf{V}_f - \mathbf{V}_a||_2}{||\mathbf{V}_a||_2} \,, \tag{5}$$

where $||\mathbf{F}||_2 = \sqrt{\sum_i F_i^2}$ denotes 2-norm.

B. Anatomical ventricular model

In the second part of this study we simulated body surface potentials following a methodology that was presented in detail elsewhere [9], [10]. First, we positioned an anatomical model of the human ventricles (Fig. 2) in the homogeneous boundary-element torso model [11] at the hearts anatomical location documented by radiographic images. Secondly, we simulated an activation sequence using a ventricular model [13] that features an anatomically accurate geometry, with a resolution of 0.5 mm, an intramural structure with rotating anisotropy and a computational implementation of a propagation algorithm based on combining a cellular automaton with bidomain models [14], [15]. From this realistic activation sequence, we calculated extra-cardiac electric potentials employing the oblique dipole model of cardiac sources in combination with the boundary element torso model [9]. The infinite medium electric potentials $\mathbf{\Phi}_\infty$ was determined from the discretized equation

$$-4\pi\sigma_0\mathbf{\Phi}_\infty = \sigma_1 \int \frac{\nabla v_m \cdot \boldsymbol{r}}{r^3} dV + \sigma_2 \int \boldsymbol{a}\boldsymbol{a}^T \frac{\nabla v_m \cdot \boldsymbol{r}}{r^3} dV \,, \tag{6}$$

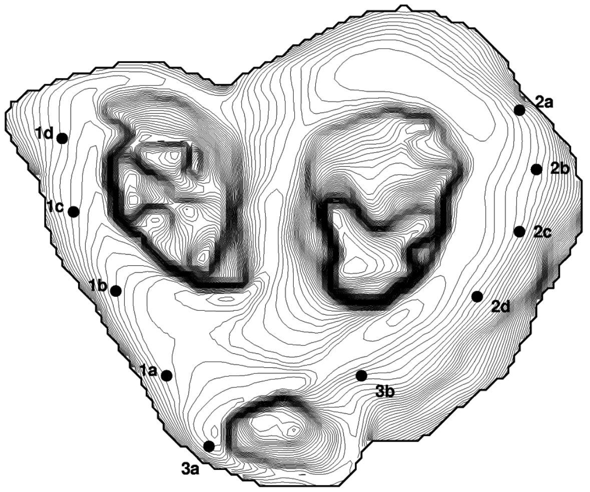

Fig. 2. Basal view of human ventricular model shown with 10 sites of accessory pathways, which are related to locations obtained with clinical studies [12]. Layers are 1 mm apart, and each is represented by smoothed contour line to achieve better rendering of shape. Accessory pathways labeled 1 are located at right anterolateral to right posterolateral region, those labeled 2 are at left posterolateral to left anterolateral region, and those labeled 3 are at right or left anteroparaseptal region (see Table III). Right ventricle is to left, left ventricle is to right, and pulmonary artery is at bottom.

where the integrals were evaluated over the ventricular volume; v_m was the transmembrane potential calculated using the propagation algorithm; σ_0 was the conductivity of the homogeneous monodomain; σ_1 and σ_2 were conductivities characterizing anisotropic myocardium; $\boldsymbol{a}$ is the local direction of the fiber axis; and $\boldsymbol{r}$ is the distance from the source point (each activated cell) to a field point. To compute the body surface potentials we used a fast forward solution [16], [17]. To account for the influence of the torsos outer boundary on localization results, we used, in addition to the standard male torso model, an individualized male torso model [9] to simulate body surface potentials generated by the ventricular model[1]. As before, the two-dipole inverse problem was solved using the standard male torso model. For each activation sequence, we simulated body surface potentials (at 117 sites on both the anterior and posterior torso) at 4 ms increments, within the first 40 ms after the onset of activation. As a measure of the accuracy of the localization, we used the localization error, defined as the three-dimensional distance between the locations of the best-fitting pair of dipoles and each of the two accessory pathways in the ventricular model.

Macchi et al. [18] and Taccardi et al. [19] pointed out that electric potentials during the initial phase of activation resemble those of two opposing dipoles oriented along the major axis and located near the ends of an elliptical wavefront of the propagated activation. To test this hypothesis, we first assessed the performance of a two-dipole generator in localizing single accessory pathways. We simulated electric potentials corresponding to sequences initiated at ten single pacing sites in the right anterolateral/posterolateral segment, in the left posterolateral/anterolateral segment, and in the right/left anteroparaseptal segment of the atrioventricular ring (Fig. 2). Using these simulated potentials, we solved the two-dipole inverse problem and specifically verified whether the positions of the reconstructed dipoles corresponded to the leading edge of the activation wavefront. The results of this study can be found in Section III-B1.

TABLE III. ANATOMICAL DESCRIPTION OF DUAL SITES

	Abbreviation	Anatomical description	Distance*
1a-1b	RAL	Right anterolateral	18
1a-1c	RAL	Right anterolateral/ right lateral	18
1a-1d	RAL/RPL	Right anterolateral/ right posterolateral	48
2a-2b	LPL/LL	Left posterolateral/ left lateral	11
2a-2c	LPL/LL	Left posterolateral/ left lateral	23
2a-2d	LPL/LAL	Left posterolateral/ left anterolateral	36
3a-3b	RAP/LAP	Right anteroparaseptal/ left anteroparaseptal	30
1b-2b	RAL/LPL	Right anterolateral/ left posterolateral	139

*Distance in mm measured along atrioventricular (AV) ring

Next, we solved the inverse problem using the sequences initiated at eight different pairs of pacing sites in the same segments of the AV ring (Fig. 2 and Table III). Gaussian noise at the root-mean-square (RMS) levels of 2.5 μV, 5 μV and 20 μV was added to all simulated body surface potentials. We generated ten different noise distributions for each noise level, and, with these data, the two-dipole inverse problem was solved. The results of this study can be found in Section III-B2.

To compare the accuracy of the two-dipole model inverse solution with that of the single-dipole inverse solution, we also calculated the inverse solution for the single-dipole model for the simulated data described above. For this inverse solution, we used methods described earlier [13]. When using the individualized male torso model, Gaussian noise at the RMS level of 5 μV was added to the simulated body surface potentials. The results of this study can be found in Section III-B3.

III. RESULTS

A. Conducting sphere model

Table IV and Fig. 3 display average single dipole source localization errors (Δr) and REs calculated with different lead system and noise levels, where

$$\Delta r = ||\vec{r}_f - \vec{r}_p||_2\,, \tag{7}$$

and $\vec{r}_f$ and $\vec{r}_p$ are fitted and original dipole locations, respectively. Results clearly show that for high *S/N* ratio (40 dB) location of the single current dipole almost coincide with the original source for all lead systems. The 32-Epi lead system outperforms the other two in terms of localization error. On the other hand, relative fit errors $\mathrm{RE_{fn}}$ are almost the same for all lead systems. Note, that fitted potential maps are more similar to the analytical maps than noisy maps ($\mathrm{RE_{fa}} < \mathrm{RE_{fn}}$).

---

[1] We altered the geometry of the outer surface of the torso and the position of the ventricular model in the torso, but did not change the size of the ventricular model.

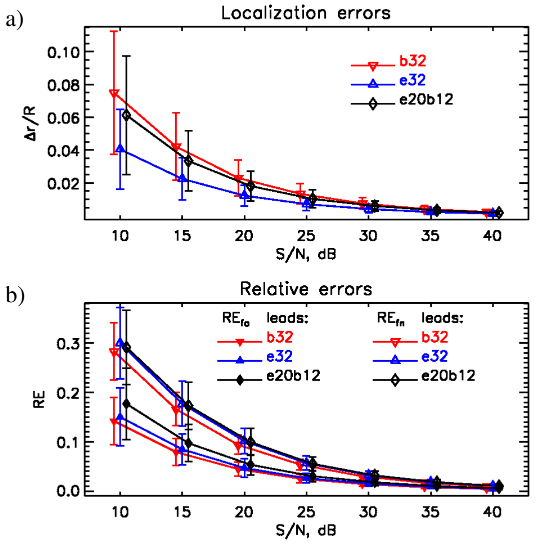

Fig. 3. a) Localization errors ($\Delta r/R$) and b) relative errors ($\mathrm{RE}_{\mathrm{fn}}$ and $\mathrm{RE}_{\mathrm{fa}}$) vs. noise levels for single dipole sources.

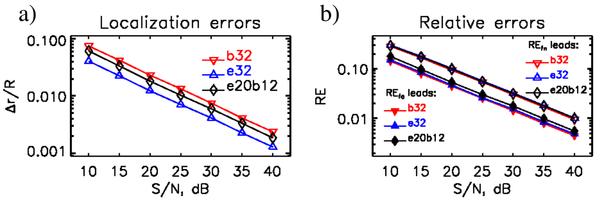

Fig. 4. Logarithmic scaling of a) localization errors and b) relative errors for single dipole sources.

Fig. 4 displays Δr and REs in logarithmic scale. We observe linear dependence of both $\log(\Delta r/R)$ and $\log(\mathrm{RE})$ vs. *S/N*. According to Eq. (4), both Δr and RE are therefore proportional to noise RMS value.

Table V displays average dual dipole source localization errors (Δr_1, Δr_2 and Δr_{c}) and REs calculated by 32-Epi lead system using data with different noise levels generated with dual dipole sources with different mutual distances and orientations. Localization errors are defined as distances between the recovered locations ($\vec{r}_{f1}$, $\vec{r}_{f2}$) and original locations ($\vec{r}_{p1}$, $\vec{r}_{p2}$) of both dipoles. Combined error is defined as

$$\Delta r_{\mathrm{c}} = \sqrt{\Delta r_1^2 + \Delta r_2^2}, \tag{8}$$

and it is shown in Fig. 5. Results show that distance between dipoles in the dual dipole source model plays an important role in the source localization procedure. In the presence of noise, locations of close positioned dipoles are poorly recovered. On the other hand, mutual orientation between dipoles is not so important.

B. Anatomical ventricular model

1) Localization of single accessory pathway using two-dipole model: Fig. 6a shows a typical example of localization of a single accessory pathway when the two-dipole model is used under ideal noise-free conditions. Localization of a pair of dipoles is shown at different time instants for an activation sequence initiated at the left lateral site (2c). Both reconstructed dipoles are initially in the sequence located close to the site of an accessory pathway, but later become separated by the distance that is progressively increasing with time. The distance between the leading edge of the simulated wavefront and the locations of the two corresponding, reconstructed dipoles is, on average, 3 mm (range 1-5 mm) during the first 28 ms of an activation sequence. This observation strongly supports the notion that progressive separation of the two dipoles reflects the propagation of an activation wavefront. Although the two-dipole model reflects well qualitative features of the propagated activation wavefront, it is less suitable for localizing the single sites of early activation than the single-dipole model. Fig. 7 comprehensively compares the accuracy of the localization when both models are used, with the evident superiority of the single-dipole model. The reason for the poorer performance of the two-dipole model is the fact that such a model, as explained above, localizes both leading edges of the activation wavefront, which are progressively moving away from the actual site of pre-excitation.

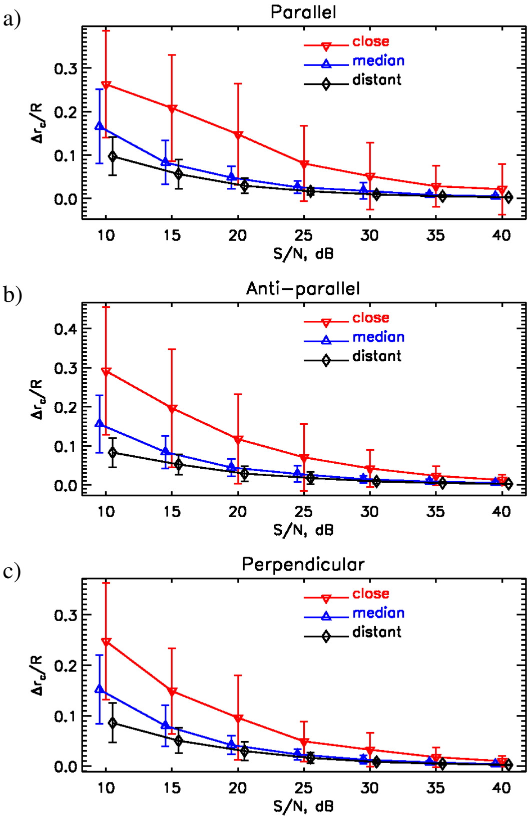

Fig. 5. Localization errors ($\Delta r_{\mathrm{c}}/R$) calculated with 32-epi lead system for dual dipole sources with a) parallel, b) anti-parallel and c) perpedicular mutual directions and different distances between dipoles that forming dual sources.

2) Localization of dual accessory pathways in presence of different noise levels: Fig. 6b illustrates localization results for the pair of right anterolateral/lateral accessory pathways with the two-dipole model. We can see that dipoles are clearly separated and located close to the actual locations of accessory pathways. In this specific case, the localization errors (±SD) attained a minimum 20 ms after the onset of activation (11±1 mm and 5±1 mm), see Table VI, where the first three columns summarize the localization results for the three noise levels. RMS

TABLE IV. SINGLE DIPOLE FIT RESULTS USING DIFFERENT LEAD SYSTEMS*

Noise	32-Body			32-Epi			12-Body-20-Epi		
[dB]	$\Delta r/R$±SD	RE$_{fn}$±SD	RE$_{fa}$±SD	$\Delta r/R$±SD	RE$_{fn}$±SD	RE$_{fa}$±SD	$\Delta r/R$±SD	RE$_{fn}$±SD	RE$_{fa}$±SD
10	0.075±0.037	0.283±0.058	0.142±0.048	0.041±0.024	0.300±0.072	0.150±0.059	0.061±0.036	0.291±0.075	0.177±0.073
20	0.023±0.011	0.094±0.019	0.045±0.014	0.012±0.006	0.101±0.026	0.047±0.019	0.018±0.009	0.099±0.027	0.053±0.021
30	0.007±0.004	0.030±0.006	0.014±0.005	0.004±0.002	0.032±0.008	0.015±0.006	0.006±0.003	0.031±0.008	0.018±0.007
40	0.002±0.001	0.009±0.002	0.004±0.002	0.001±0.001	0.010±0.003	0.005±0.002	0.002±0.001	0.010±0.003	0.006±0.002

* Averaged over 720 samples (72 single dipole sources × 10 random noise distributions) for different lead systems and noise levels.

TABLE V. DUAL DIPOLE FIT RESULTS USING 32-EPI LEAD SYSTEM**

	S/N	Parallel dipoles					Anti-parallel dipoles					Perpendicular dipoles				
	[dB]	$\Delta r_1/R$	$\Delta r_2/R$	$\Delta r_c/R$±SD	RE$_{fn}$	RE$_{fa}$	$\Delta r_1/R$	$\Delta r_2/R$	$\Delta r_c/R$±SD	RE$_{fn}$	RE$_{fa}$	$\Delta r_1/R$	$\Delta r_2/R$	$\Delta r_c/R$±SD	RE$_{fn}$	RE$_{fa}$
close	10	0.163	0.162	0.262±0.123	0.223	0.206	0.197	0.204	0.291±0.163	0.590	1.389	0.160	0.161	0.247±0.115	0.300	0.293
	20	0.093	0.088	0.148±0.116	0.077	0.063	0.081	0.080	0.117±0.114	0.346	0.409	0.063	0.060	0.096±0.083	0.108	0.086
	30	0.033	0.031	0.051±0.077	0.025	0.020	0.029	0.029	0.042±0.047	0.149	0.128	0.022	0.021	0.033±0.034	0.034	0.027
	40	0.013	0.013	0.021±0.058	0.008	0.006	0.009	0.008	0.012±0.013	0.050	0.038	0.007	0.007	0.010±0.010	0.011	0.008
median	10	0.116	0.101	0.166±0.086	0.199	0.177	0.122	0.086	0.156±0.074	0.363	0.345	0.117	0.086	0.152±0.068	0.249	0.229
	20	0.033	0.031	0.048±0.026	0.068	0.054	0.030	0.030	0.045±0.022	0.134	0.106	0.030	0.026	0.042±0.018	0.088	0.067
	30	0.010	0.013	0.018±0.019	0.022	0.017	0.010	0.010	0.015±0.009	0.043	0.032	0.009	0.008	0.013±0.009	0.028	0.021
	40	0.003	0.003	0.005±0.003	0.007	0.005	0.003	0.003	0.005±0.004	0.013	0.011	0.003	0.003	0.004±0.002	0.008	0.007
distant	10	0.061	0.068	0.097±0.044	0.183	0.148	0.051	0.059	0.083±0.037	0.224	0.183	0.055	0.059	0.086±0.039	0.199	0.160
	20	0.018	0.021	0.029±0.018	0.059	0.047	0.017	0.021	0.029±0.019	0.075	0.057	0.018	0.021	0.030±0.018	0.065	0.051
	30	0.006	0.006	0.009±0.005	0.019	0.015	0.005	0.006	0.009±0.005	0.024	0.018	0.005	0.006	0.008±0.004	0.021	0.016
	40	0.002	0.002	0.003±0.001	0.006	0.005	0.002	0.002	0.003±0.001	0.007	0.006	0.002	0.002	0.003±0.001	0.007	0.005

** Averaged over 360 samples (36 dual dipole sources × 10 random noise distributions) for different *S/N* and groups of distances and orientations between two single dipoles that forming dual dipole sources.

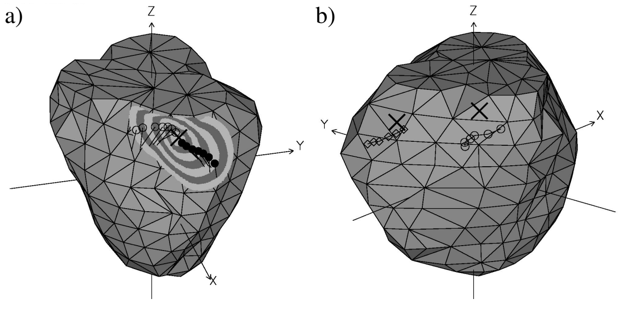

Fig. 6. a) Localization of left-lateral single accessory pathway. Inverse solutions were performed under no-noise conditions. (×) Onset of accessory pathway; reconstructed positions: (○) first and (●) second dipoles, where short lines indicate directions of reconstructed dipole moments. Alternating light and dark gray zones represent projection of activation isochronal surface on epicardial surface, 4-28 ms after onset of activation.
b) Localization of right anterolateral/right lateral (case 1a-1c) dual accessory pathway using two-dipole model. Positions of two dipoles reconstructed at different time instants, 16-36 ms after onset of activation, are shown with epicardial surface. Inverse solutions were obtained with Gaussian RMS noise of 5 μV added to simulated body surface potentials. (×) Onset of each accessory pathway; reconstructed dipoles: (○) first and (◇) second dipoles.

levels of the simulated body surface potentials were, at 20 ms after the onset of activation, between 104 μV (case 2a-2b) and 164 μV (case 1a-1c). We found that two-dipole localization errors for typical measuring conditions (RMS noise level of 5 μV) reached a minimum between 12 ms and 24 ms after the onset of activation (Fig. 8). For such measuring conditions, the average localization errors were between 5 and 21 mm (12±6/11±6 mm at 20 ms for the first/second dipole, respectively). Localization errors were, on average, smaller for the pairs of accessory pathways located on the right side (8 mm for cases 1a-1b, 1a-1c, 1a-1d) than for those located on the left side (14 mm for cases 2a-2b, 2a-2c, 2a-2d).

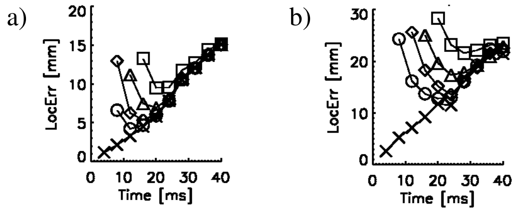

Fig. 7. Localization errors a) for a single dipole source and b) for a two-dipole source model averaged over 8 single accessory pathways, 4-40 ms after onset in presence of different noise levels: (×) no noise; (○) RMS noise level of 2.5 mV; (◇) 5 mV; (△) 10 mV; (□) 20 mV.

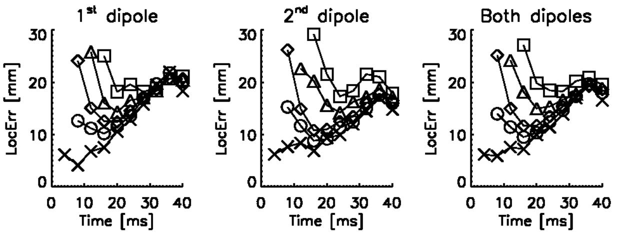

Fig. 8. Localization errors for dual accessory pathway with two-dipole source in presence of different noise levels: (×) no noise; (○) RMS noise level of 2.5 mV; (◇) 5 mV; (△) 10 mV; (□) 20 mV.

3) Localization of dual accessory pathways in the presence of modeling errors: Localization errors due to inaccuracies in rendering individualized torso boundaries (i.e. in the presence of modeling errors) were, in general, larger than those due to noise and reached their minimum between 16 and 28 ms after the onset (the last column in Table VI). The errors were, on average, in the range of 11-39 mm (24±18/30±13 mm at 20 ms) for the body surface potentials. Visual inspection of inversely calculated dipole positions revealed that they were often distal to the actual locations of accessory pathways and sometimes fell outside anatomically plausible (ventricular) region.

TABLE VI. ACCURACY IN LOCALIZING DUAL ACCESSORY PATHWAYS IN PRESENCE OF DIFFERENT NOISE SOURCES*

Abbr.	2.5 μV first / second dipole (time)	5 μV first / second dipole (time)	20 μV first / second dipole (time)	Modeling noise & 5 μV first / second dipole (time)
1a-1b	7±2 / 5± 2 mm (16 ms)	9± 3 / 7±3 mm (16 ms)$^{10\%}$	13± 5 / 18± 7 mm (20 ms)	22±10 / 20± 5 mm (24 ms)
1a-1c	10±1 / 5±0.4 mm (20 ms)	11± 1 / 5±1 mm (20 ms)	15± 3 / 12± 3 mm (28 ms)$^{10\%}$	23± 3 / 22± 2 mm (28 ms)
1a-1d	9±5 / 4± 2 mm (8 ms)	11± 6 / 5±1 mm (12 ms)	20± 7 / 8± 4 mm (20 ms)	17± 1 / 27± 4 mm (28 ms)
2a-2b	11±3 / 9± 4 mm (16 ms)$^{20\%}$	21±10 / 11±4 mm (24 ms)$^{20\%}$	17± 8 / 20± 7 mm (28 ms)$^{10\%}$	39± 9 / 18±10 mm (16 ms)$^{50\%}$
2a-2c	12±5 / 12± 10 mm (16 ms)$^{30\%}$	19±12 / 8±6 mm (20 ms)$^{30\%}$	19± 5 / 21±10 mm (28 ms)$^{20\%}$	18± 9 / 36±18 mm (16 ms)$^{50\%}$
2a-2d	10±4 / 11± 6 mm (16 ms)$^{40\%}$	14± 9 / 13±5 mm (16 ms)$^{30\%}$	22±11 / 19±10 mm (24 ms)$^{30\%}$	19±12 / 34±16 mm (16 ms)$^{50\%}$
1b-2b	5±1 / 6± 1 mm (12 ms)	7± 2 / 8±3 mm (16 ms)	13± 4 / 19±10 mm (20 ms)	16± 2 / 11± 4 mm (16 ms)
3a-3b	10±2 / 6± 3 mm (20 ms)	11± 2 / 10±6 mm (20 ms)	15± 4 / 11± 8 mm (32 ms)$^{20\%}$	11± 5 / 23± 7 mm (28 ms)$^{10\%}$
All sites	10±4 / 9± 7 mm (16 ms)$^{11\%}$	12± 6 / 11±6 mm (20 ms)$^{10\%}$	18± 8 / 18± 9 mm (20 ms)$^{12\%}$	24±18 / 30±13 mm (28 ms)$^{9\%}$

*Three-dimensional distances (±SD) between each of two accessory pathways and two reconstructed dipoles are shown. In the first three columns standard torso model was used for the forward solution with different Gaussian noise RMS level of 2.5, 5 and 20 μV. In the last column the individualized torso model was used for the forward problem solution with Gaussian noise RMS level of 5 μV. The standard torso model was used for the inverse problem solution in all cases. See Table III for anatomical descriptions of accessory pathways. Label N% indicates rejected inverse solutions as percentage of total number of inverse solutions. We rejected all solutions for which the magnitude of the stronger of the two dipoles exceeded the weaker dipole by a factor of 5.

IV. CONCLUSIONS

In this simulation study, we revisited a well-known bio-electromagnetic model that substitutes true cardiac sources with idealized equivalent single and dual dipole sources. We constructed a simplified analytically solvable source and volume conductor model for evaluation electrocardiographic inverse problem solutions. Both fitted single current dipoles and dual current dipoles virtually coincided with the original source for high S/N ratios. In the presence of higher noise we found that i) lead systems positioned closer to sources are more efficient and ii) dual current dipole location recovery is sensitive to the distance between the original dipoles.

Our anatomical model of the human ventricles provided us with means to investigate quantitatively the performance of such a model for more realistic electrocardiographic inverse solutions. The results of this study demonstrate that a source model consisting of two dipoles embedded in the realistically shaped torso volume conductor model could be useful in localizing dual accessory pathways providing that i) we know the torso geometry of a given patient ii) we have a priori knowledge of the presence of dual accessory pathways. Both aspects need to be determined non-invasively to be of clinical use.

REFERENCES

[1] P. Savard, F. A. Roberge, and R. M. Gulrajani, "A simulation study of the single moving dipole representation of cardiac electrical activity," *IEEE Trans. Biomed. Eng.*, vol. BME-29, pp. 700–707, 1982.

[2] R. M. Gulrajani, F. A. Roberge, and P. Savard, "Moving dipole inverse ECG and EEG solutions," *IEEE Trans. Biomed. Eng.*, vol. BME-31, pp. 903–910, 1984.

[3] T. F. Oostendorp and A. van Oosterom, "Source parameter estimation in inhomogeneous volume conductors of arbitrary shape," *IEEE Trans. Biomed. Eng.*, vol. BME-36, no. 3, pp. 382–391, 1989.

[4] J. de Guise, R. M. Gulrajani, P. Savard, and R. G. F. A. Roberge, "Inverse recovery of two moving dipoles from simulated surface potential distributions on a realistic human torso model," *IEEE Trans. Biomed. Eng.*, vol. BME–32, pp. 126–135, 1985.

[5] J. H. McClelland, K. J. Beckman, X. Wang, H. A. Hazlitt, M. I. Prior, N. Twindale, K. P. Moulton, C. A. Roman, R. Lazzara, and W. M. Jackman, "Radiofrequency ablation elucidates accessory pathway anatomy," *Circulation*, vol. 84, pp. II–24, 1991.

[6] I. Singer, *Intervantional electrophysiology*. Baltimore: Williams and Wilkins, 1997.

[7] D. Yao, "Electric potential produced by a dipole in a homogeneous conducting sphere," *IEEE Trans. Biomed. Eng.*, vol. BME-44, pp. 964–966, 2000.

[8] D. A. Brody, F. H. Terry, and R. E. Ideker, "Eccentric dipole in a spherical medium: Generalized expressio n for surface potentials," *IEEE Trans. Biomed. Eng.*, vol. BME-20, pp. 141–143, 1973.

[9] R. Hren, G. Stroink, and B. M. Horáček, "Spatial resolution of body surface potential maps and magnetic field maps: A simulation study applied to the identification of ventricular preexcitation sites," *Med. Biol. Eng. Comp.*, vol. 36, pp. 145–157, 1998.

[10] V. Jazbinšek, R. Hren, G. Stroink, B. M. Horáček, and Z. Trontelj, "Value and limitations of an inverse solution for two equivalent dipoles in localising dual accessory pathways," *Med. Biol. Eng. Comp.*, vol. 41, pp. 133–140, 2003.

[11] B. M. Horáček, "Numerical models of inhomogeneous human torso," *Adv. Cardiol.*, vol. 10, pp. 51–57, 1974.

[12] P. Iturralde, M. Guevara-Valdivia, L. Rodríguez-Chávez, A. Medeiros, and L. Colin, "Radiofrequency ablation of multiple accessory pathways," *Europace*, vol. 4, pp. 273–280, 2002.

[13] R. Hren, G. Stroink, and B. M. Horáček, "Accuracy of single-dipole inverse solution when localising ventricular pre-excitation sites: simulation study," *Med. Biol. Eng. Comp.*, vol. 36, pp. 323–329, 1998.

[14] L. J. Leon and B. M. Horáček, "Computer model of excitation and recovery in the anisotropic myocardium. I. rectangular and cubic arrays of excitable elements," *J. Electrocardiol.*, vol. 24, pp. 1–15, 1991.

[15] J. Nenonen, J. A. Edens, L. J. Leon, and B. M. Horáček, "Computer model of excitation and recovery in the anisotropic myocardium. i. rectangular and cubic arrays of excitable elements," in *Computers in Cardiology*, A. Murray and R. Arzbacher, Eds. Los Alamitos: IEEE Computer Society, 1991, pp. 545–548.

[16] C. J. Purcell and G. Stroink, "Moving dipole inverse solutions using realistic torso models," *IEEE Trans. Biomed. Engr.*, vol. BME-38, pp. 82–84, 1991.

[17] J. Nenonen, C. J. Purcell, B. M. Horacek, G. Stroink, and T. Katila, "Magnetocardiographic functional localization using a current dipole in a realistic torso," *IEEE Trans. Biomed. Eng.*, vol. BME-38, no. 7, pp. 658–664, 1991.

[18] E. Macchi, G. Arisi, and B. Taccardi, "Identification of ectopic ventricular foci by means of intracavitary potential mapping: a proposed method," *Acta Cardiol.*, vol. 47, pp. 421–433, 1992.

[19] B. Taccardi, E. Macchi, R. L. Lux, P. R. Ershler, S. Spaggiari, S. Baruffi, and Y. Vyhmeister, "Effect of myocardial fiber direction on epicardial potentials," *Circulation*, vol. 90, pp. 3076–3090, 1994.